ANNALS of Faculty Engineering Hunedoara – International Journal of Engineering
Tome XVIII [2020] | Fascicule 4 [November]

ANNALS of Faculty Engineering Hunedoara – International Journal of Engineering
ISSN 1584 - 2665 (printed version); ISSN 2601 - 2332 (online); ISSN-L 1584 - 2665

[1.]Alexandru IONEL

SOLID ROCKET MOTOR STAR GRAIN GEOMETRICAL ANALYSIS AND PERFORMANCE MODEL

[1.] INCAS, National Institute for Aerospace Research 'Elie Carafoli', Bucharest, ROMANIA

Abstract: This paper analyzes the influence of grain star port configuration on the performance of solid rocket motors. SRM grain performance parameters are plotted for different combinations of geometric parameters of the star port section. A numerical simulation is performed in MATLAB to solve the SRM internal ballistics model coupled with the port and burning areas geometric build-up. Results show the importance of each geometrical parameter that define the star port SRM grain section.
Keywords: solid rocket motor; star grain; interior ballistics; unsteady flow; MATLAB

1. INTRODUCTION

The invention and development of the rocket is linked with commerce, transportation, war, and ultimately, human, and civilization development. Rockets have been used in wars since 1275, and now, in the new millennium, the rocket is envisioned as a transportation revolution. Although a small number of people travelled in vehicles propelled by rockets, the majority of domestic and commercial communications rely on satellites, which are sent to orbit via rockets [1]. In addition, the Mars exploration program cannot be made possible without the use of rocket propulsion. Consequently, rockets are key, as far as space commerce, science, and exploration. Rockets can be classified as non-chemical and chemical. Chemical rockets are heat engines that convert the heat generated by combustion of propellant, into kinetic energy of the exhaust gas. The exhaust gas momentum provides thrust that accelerates the rocket. Chemical rockets can be solid propellant rocket motors (SPRM), liquid propellant engines (LPRM), hybrid propellant motors and gel rocket motors. Because the liquid propellant rocket engine is fairly complicated in design, more attention was given to the solid propellant motor development, although a SPRM functions thermodynamically the same way as a LPRM - combustion produces hot gas, accelerated by the exhaust nozzle. The propellant form is different, with the fuel and oxidant being pre-mixed in solid form, and cast in the combustion chamber. Combustion produces hot gas on the surface of the propellant [2]. The combustion chamber of a SPRM is much simpler than in the case of a LPRM. It consists of a casing for the propellant, continued by a nozzle. After ignition, the motor continues to produce thrust until the propellant is exhausted. Design issues are concerned with selection of propellant type and mounting of the solid propellant inside the casing. In terms of cooling techniques, heat dissipation has to be entirely passive. Thrust stability in a SPRM is a serious issue because there are many chances for instabilities to appear and propagate. While the SPRM is essentially single-use, because the cost of large boosters is very high and the necessary engineering quality of its components, boosters are recovered and segments reused [3].

Solid propellant grains with star section configuration are extensively used for the propulsion of launch vehicles, missiles, and rockets. For the evaluation of burn area variation, several parameters are of importance. Burn rate influence: pressure level rises along with burn rate, while the burning duration reduces.

Additionally, tail-off duration reduces significantly with rise in burn rate, but at the same time, total burn duration also reduces and tail-off factor remains constant. Throat diameter influence: higher pressure arises with reduced throat area but effect of throat area on the neutrality factor is negligible. The tail-off duration increases with increase in throat diameter, but simultaneous rise in total burn time offsets the effect to give tail-off factor also independent of throat diameter. Angular fraction influence: increasing the angular fraction results in reduced thickness of the star port. High angular fraction usually means high peak and neutral pressure [4]. Higher angular fraction values result in reduced neutrality factor. Tail-off duration and total burning time rise along with total time of burning. Star outer diameter influence: this parameter can be changed as part of propellant design, and results in reduced propellant weight. Large star outer diameter results in neutral pressure-time profile and increased tail-off duration. Along with increased star outer diameter, neutrality factor reduces, peak pressure increases, tail-off duration increases and total burning time reduces. Star angle influence: at lower than neutral angles, the pressure-time profile is M shaped, and for higher than neutral angle values, the pressure-time profile monotonically rises to peak pressure. For higher star angle, minimum pressure is much lower and neutrality factor is adversely affected. Tail-off factor is not affected by star angle [5].

2. PERFORMANCE MODEL

It is necessary to treat the rocket motor as an ideal heat engine to define the equations that construct the internal ballistics model of the motor. This ideal model is based on these assumptions: the flow is 1D; the perfect gas laws apply to the combustion products; the burn gases have constant specific heat; friction is neglected; boundary layer effects are neglected; combustion gases are homogenous; exhaust gases have only axial velocity; the burning process is unsteady in time; no discontinuities and shock waves in the exhaust nozzle; the flow is adiabatic; combustion chamber complete combustion; uniformity of gas density, temperature, pressure, and velocity, in any section [6].

Thrust is the main design constraint of the propulsion system. Thrust can be calculated from the momentum equation applied on the overall rocket system. Thrust is calculated with (1), where $\Gamma(\gamma)$ is Vanderckove's function, γ is the adiabatic coefficient, P_c is the combustion chamber pressure, A_t is the throat area, v_e is the exhaust velocity, R is the gas constant, T_c is the chamber temperature, A_e is the exhaust nozzle exit area, P_e is the exhaust nozzle exit area, and P_a is the atmospheric pressure.

$$\mathrm{Tr} = \frac{\Gamma(\gamma) P_c A_t v_e}{\sqrt{R T_c}} + A_e (P_e - P_a) \tag{1}$$

An important parameter of the rocket motor is A_e, the cross-sectional area of the exit station of the nozzle. The velocity profile is difficult to measure accurately since the actual exhaust velocity is not uniform over the entire exit cross-section and does not represent the entire thrust magnitude. A uniform axial velocity is assumed which allows a one-dimensional description of the problem. (2) define the effective exhaust velocity.

$$v_e = \sqrt{\frac{2}{\gamma - 1} R T_c \left[1 - \left(\frac{P_e}{P_c}\right)^{\frac{\gamma-1}{\gamma}}\right]} \tag{2}$$

The specific impulse, I_{sp}, is a measure of the impulse or momentum change that can be produced per unit mass of the propellant consumed, i.e., the ratio of thrust to the propellant weight flow per second. The specific impulse is defined by (3), in which C_t is the thrust coefficient, and C_D is the characteristic velocity.

$$I_{sp} = C_T C_D \tag{3}$$

The thrust coefficient, C_t represents the performance of the nozzle for a fixed propellant configuration. Thrust coefficient is defined as the thrust divided by the chamber pressure, P_c and the throat area A_t. The thrust coefficient C_t, calculated with (4) and (5), is a function of gas property, nozzle expansion ratio, nozzle pressure ratio and atmospheric pressure.

$$C_T^0 = \Gamma(\gamma) \sqrt{\frac{2\gamma}{\gamma - 1}\left[1 - \left(\frac{P_e}{P_0}\right)^{\frac{\gamma-1}{\gamma}}\right]} \tag{4}$$

$$C_T = C_T^0 + \frac{A_e}{A_{cr}}\left(\frac{P_e}{P_0} - \frac{P_a}{P_0}\right) \tag{5}$$

Characteristic velocity c* is a function of the propellant characteristics and combustion chamber design. It is independent of nozzle characteristics. The c* is used in comparing the relative performance of different chemical rocket propulsion system designs and propellants. It measures the efficiency of conversion of thermal energy in the combustion chamber into high-velocity exhaust gas [7]. The c* can be formulated as in (6):

$$c^* = \frac{\sqrt{RT_c}}{\Gamma} = \frac{1}{C_D} \rightarrow T_c = \frac{(c^*\Gamma)^2}{R} \tag{6}$$

The size of the throat area, A_t, is one of the main parameters of rocket size. The defining property of the nozzle is the exit area, A_e, and the shape of the nozzle can be expressed in a dimensionless way as the expansion ratio, ε, (7). (8) provides a way of determining the exhaust nozzle exit pressure

$$A_e = \varepsilon A_t \tag{7}$$

$$\frac{A_e}{A_{cr}} = \frac{\Gamma(\gamma)}{\left(\frac{P_e}{P_0}\right)^{\frac{1}{\gamma}}\sqrt{\frac{2\gamma}{\gamma-1}\left[1-\left(\frac{P_e}{P_0}\right)^{\frac{\gamma-1}{\gamma}}\right]}} \rightarrow P_e \tag{8}$$

Chamber pressure is the gas pressure inside the combustion chamber during motor operation. The chamber pressure can be obtained using (9):

$$\frac{dP_c}{dt} = \frac{(c^*\Gamma)^2}{V_c}\left[(\rho_p - \rho_c)A_b\dot{r}_b - \frac{P_c A_t}{c^*}\right] \tag{9}$$

Burning rate: the burning surface of a propellant grain recedes in a direction perpendicular to the surface. Aside from the propellant formulation and propellant manufacturing process, burning rate in a full-scale motor can be increased by the following: combustion chamber pressure; initial temperature of the solid propellant; combustion gas temperature; velocity of the gas flow parallel to the burning surface. The burning rate of propellant in the motor is shown in (10). In (10), T_i is the grain initial temperature, and T_{ref} is the reference temperature of 288K.

$$r_b(p,T) = 6.2062 - 3e^{0.0018(T_i - T_{ref})}p^{0.0382} \tag{10}$$

3. GEOMETRIC ANALYSIS

The grain burnback phenomenon consists of calculating the burn surface evolution during solid rocket motor firing. Because of combustion, the burning surface recedes, propagating radially. Grain burnback has a strong influence on the SRM performance, because it is linked to the internal ballistics of the motor. The internal ballistics model has input from the grain regression model, the burning surface, the port area, and the chamber burning volume [8]. From a mathematical perspective, the problem which needs to be resolved is the burning surface evolution prediction [9]. The burning rate depends on time, burning surface normal propagation, and the chamber pressure. For the geometrical analysis of the star section grain, the methodology from [10] was used. For verification purposes, Catia v5R21 software was used for the geometrical build-up. The burning areas were calculated in MATLAB software, as part of the internal ballistics model. Input data for the star grain section are usually in the form of the following defining geometric parameters: N – number of star points, R_e – grain exterior radius, R_i – grain interior radius, ε– angular fraction, f – grain section fillet radius. The goal is by using these geometrical elements to arrive at the burn perimeter for each burning phase, as described in Figure 1. The grain section shapes for these perimeters will be formed of circle arcs and lines, depending on the burn phase.

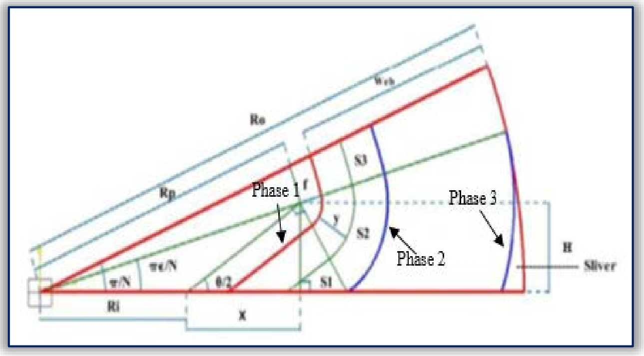

Figure 1. The star grain section – main geometrical parameters and specific burn phases

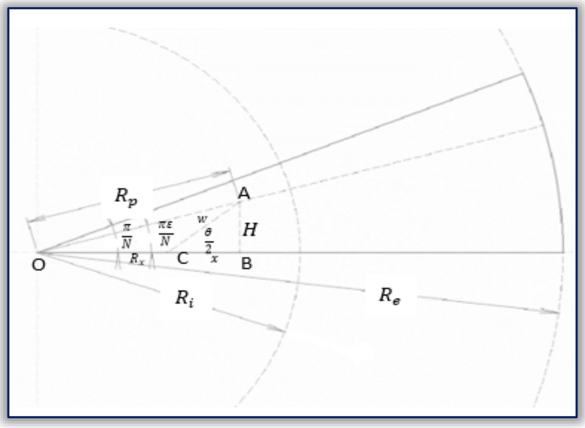

Figure 2 Additional geometrical parameters needed for describing burn phase 1 of the star grain section

To define the burn perimeter shape in phase 1, we need additional geometrical elements, which are found by using the input geometrical parameters, Re, Ri, eps, n, and f. Starting, of interest is the $\theta/2$ angle from Figure 2, which is resolved by using (11-15).

$$\sin\frac{\pi\varepsilon}{N} = \frac{H}{R_p} \Leftrightarrow H = R_p \sin\frac{\pi\varepsilon}{N} \tag{11}$$

$$\tan\frac{\pi\varepsilon}{N} = \frac{H}{R_x + x} \Leftrightarrow H = (R_x + x)\tan\frac{\pi\varepsilon}{N} \tag{12}$$

$$R_p \sin\frac{\pi\varepsilon}{N} = (R_x + x)\tan\frac{\pi\varepsilon}{N} \Leftrightarrow \frac{R_p \sin\frac{\pi\varepsilon}{N}}{\tan\frac{\pi\varepsilon}{N}} - R_x = x \tag{13}$$

$$\tan\frac{\theta}{2} = \frac{H}{x} = \frac{R_p \sin\frac{\pi\varepsilon}{N}}{\frac{R_p \sin\frac{\pi\varepsilon}{N}}{\tan\frac{\pi\varepsilon}{N}} - R_x} = \frac{R_p \sin\frac{\pi\varepsilon}{N}\tan\frac{\pi\varepsilon}{N}}{R_p \sin\frac{\pi\varepsilon}{N} - R_x \tan\frac{\pi\varepsilon}{N}} \tag{14}$$

$$\frac{\theta}{2} = \tan^{-1}\frac{R_p \sin\frac{\pi\varepsilon}{N}\tan\frac{\pi\varepsilon}{N}}{R_p \sin\frac{\pi\varepsilon}{N} - R_x \tan\frac{\pi\varepsilon}{N}} \tag{15}$$

Figure 3 shows the needed geometrical variables for the determination of the phase 1 burn shape, defined by the S1, S2, and S3 elements. These lengths are calculated using (17-20). Although the calculations above express relationships between geometrical elements in one section of the star grain shape, the values for the burn, and free areas described in (22-23) are for the whole grain length. The maximum grain thickness burned in phase 1 can be calculated using (16).

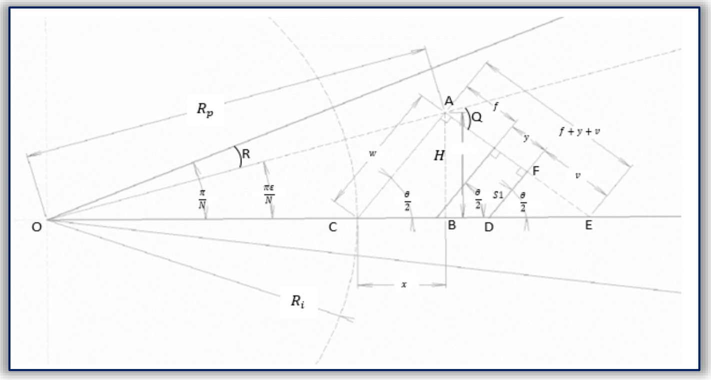

Figure 3. Star grain section geometrical build-up and main parameters of the burn phase 1

$$y_{1_{max}} = \frac{R_p \sin\frac{\pi\varepsilon}{N}}{\cos\frac{\theta}{2}} - f \tag{16}$$

$$\tan\frac{\theta}{2} = \frac{v}{S_1} \Leftrightarrow v = S_1 \tan\frac{\theta}{2} \tag{17}$$

$$\cot\frac{\theta}{2} = \frac{w}{f+y+v} \Leftrightarrow \cot\frac{\theta}{2} = \frac{w}{f+y+S_1\tan\frac{\theta}{2}} \Leftrightarrow S_1 = w - \cot\frac{\theta}{2}(f+y) \Leftrightarrow S_1 = \frac{R_p \sin\frac{\pi\varepsilon}{N}}{\sin\frac{\theta}{2}} - \cot\frac{\theta}{2}(f+y) \tag{18}$$

$$S_2 = (y+f)Q = (y+f)\left(\pi - \left(\frac{\pi}{2} - \frac{\pi\varepsilon}{N}\right) - \frac{\theta}{2}\right) \tag{19}$$

$$S_3 = \left(y + f + R_p\right)\left(\frac{\pi}{N} - \frac{\pi\varepsilon}{N}\right) \tag{20}$$

$$S_{p1} = 2N(S_1 + S_2 + S_3) \tag{21}$$

$$A_{s1} = S_{p1}L \tag{22}$$

$$A_{p1} = 2N\left\{\frac{1}{2}R_p \sin\frac{\pi\varepsilon}{N}\left[R_p \cos\frac{\pi\varepsilon}{N} + R_p \sin\frac{\pi\varepsilon}{N}\tan\left(\frac{\theta}{2}\right) - \frac{1}{2}\left[\frac{R_p \sin\frac{\pi\varepsilon}{N}}{\sin\left(\frac{\theta}{2}\right)} - (y+f)\cot\frac{\theta}{2}\right]^2 \tan\frac{\theta}{2} + \frac{1}{2}(y+f)^2\left[\frac{\pi}{2} + \frac{\pi\varepsilon}{N} - \frac{\theta}{2}\right] + \frac{1}{2}\left(y+f+R_p\right)^2\left[\frac{\pi}{2} - \frac{\pi\varepsilon}{N}\right]\right]\right\} \tag{23}$$

As it can be seen form Figure 4., at the end of Phase 1 of burning, S1 diminishes, and the burning section shape will be formed of only S2 and S3.

For the second burn phase, according to Figure 5, there are only two elements forming the burning section shape. The burn areas will be calculated with equations (25-29). The thickness of the grain in phase 2 of the burn will be calculated with (24).

$$\gamma = \tan^{-1}\left(\frac{\sqrt{(y+f)^2 - H^2}}{H}\right) \tag{24}$$

$$S_2 = (y+f)Q = (y+f)\left(\pi - \left(\frac{\pi}{2} - \frac{\pi\varepsilon}{N}\right) - G\right) \tag{25}$$

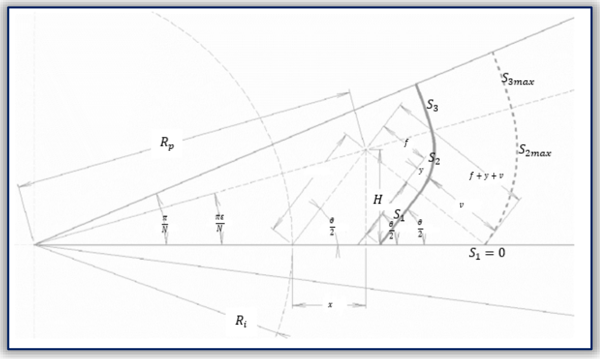

Figure 4. Star grain section geometrical parameters and limits of burn phase 1

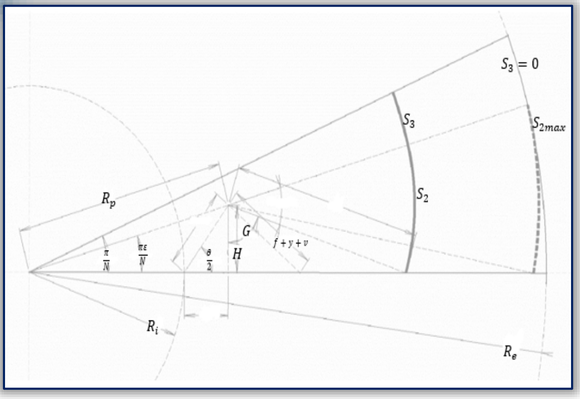

Figure 5. Star grain section geometrical parameters and limits of burn phase 2

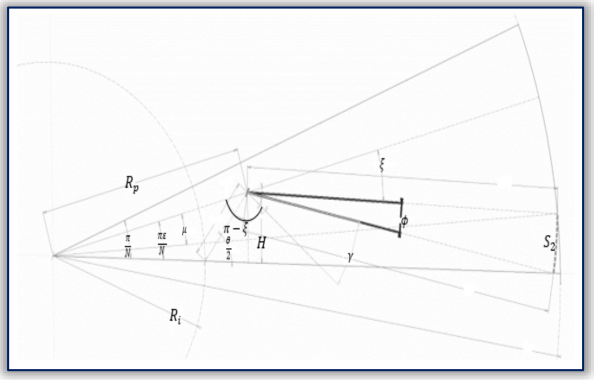

Figure 6. Star grain section geometrical parameters and limits of burn phase 3

$$S_3 = \left(y + f + R_p\right)\left(\frac{\pi}{2} - \frac{\pi\varepsilon}{N}\right) \tag{26}$$

$$S_{p2} = 2N(S_2 + S_3) \tag{27}$$

$$A_{s2} = S_{p2}L \tag{28}$$

$$A_{p2} = 2N\left\{\frac{1}{2}\left[\frac{\pi}{2} + \frac{\pi\varepsilon}{N} - \tan^{-1}\left(\frac{\sqrt{(f+y)^2 - H^2}}{H}\right)\right](y + f)^2 + \frac{1}{2}\cot\frac{\pi\varepsilon}{N}H^2 + \frac{1}{2}H\sqrt{(y+f)^2 - H^2} + \frac{1}{2}\left(R_p + f + y\right)^2\left(\frac{\pi}{N} - \frac{\pi\varepsilon}{N}\right)\right\} \tag{29}$$

For the Phase 3 of the burn, there will be only S3, according to Figure 6. S3 length will be calculated with equations (30-36), and the burn areas with (37-38).

$$\gamma = \tan^{-1}\left(\frac{\sqrt{(y+f)^2 - H^2}}{H}\right) - \frac{\theta}{2} \tag{30}$$

$$\xi = \pi - \cos^{-1}\left(\frac{{R_e}^2 - {R_p}^2 - (y+f)^2}{-2R_p(y+f)}\right) \tag{31}$$

$$\phi = \pi - \left(\frac{\pi}{2} - \frac{\pi\varepsilon}{N} + \frac{\theta}{2} + \gamma + \xi\right) \tag{32}$$

$$\mu = \cos^{-1}\left(\frac{-{R_e}^2 - {R_p}^2 + (y+f)^2}{-2R_pR_e}\right) \tag{33}$$

$$\beta = \frac{\pi}{2} - \frac{\theta}{2} + \frac{\pi\varepsilon}{N} \tag{34}$$

$$S_3 = (y + f)\phi \tag{35}$$

$$S_{p3} = 2NS_3 \tag{36}$$

$$A_{s3} = S_{p3}L \tag{37}$$

$$A_{p3} = \left\{{R_p}^2\left[\frac{\pi}{N}(1 - \varepsilon) + \mu\right] + (f + y)^2(\beta - \gamma - \xi) + R_p\sin\frac{\pi\varepsilon}{N}\left[R_p\cos\frac{\pi\varepsilon}{N} + \sqrt{(f+y)^2 - \left(R_p\sin\frac{\pi\varepsilon}{N}\right)^2}\right] - R_p\sin\mu\left[R_p\cos\mu + \sqrt{(f+y)^2 - \left(R_p\sin\mu\right)^2}\right]\right\} \tag{38}$$

4. RESULTS AND DISCUSSION

Using the SRM internal ballistics model described in equations (1-10), and the geometrical analysis model from above, the star grain section geometrical parameters influence on SRM grain performance can be determined. Of interest is the variation in time of SRM performance variables, and the best performance combination of the geometric variables.

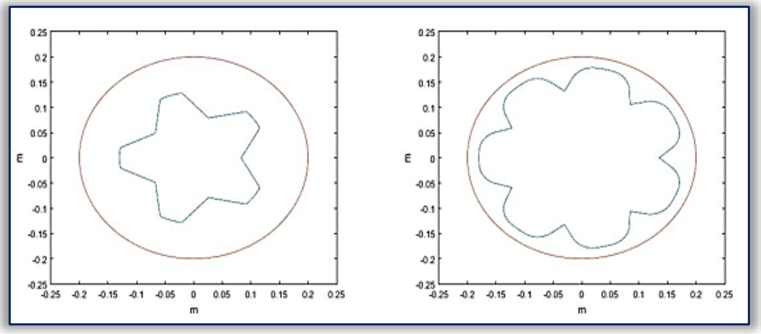

Figure 7. Star grain section examples of varying main geometrical parameters

In Figure 7, examples of combining different values of the star grain section geometrical parameters are given.

In Figure 8 – left, the port area variation with time is shown, for different angular fraction values. As it can be seen, smaller angular fraction values lead to larger port areas. In Figure 8 – right, the burning surface variation with time is shown, for different angular fraction values. As it can be seen, larger angular fraction values lead to larger burning surface values.

In Figure 9 – left, the port area variation with time is shown, for different star points number. As it can be seen, more star points lead to smaller port areas. In Figure 9 – right, the burning surface variation with time is shown, for different star points number. As it can be seen, more star points lead to smaller burning surface values.

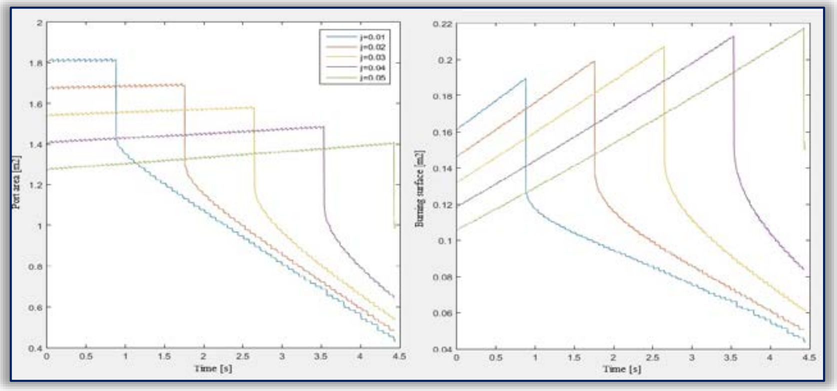

Figure 8. Port area variation with time for different angular fraction values (left); burning surface variation with time for different angular fraction values (right)

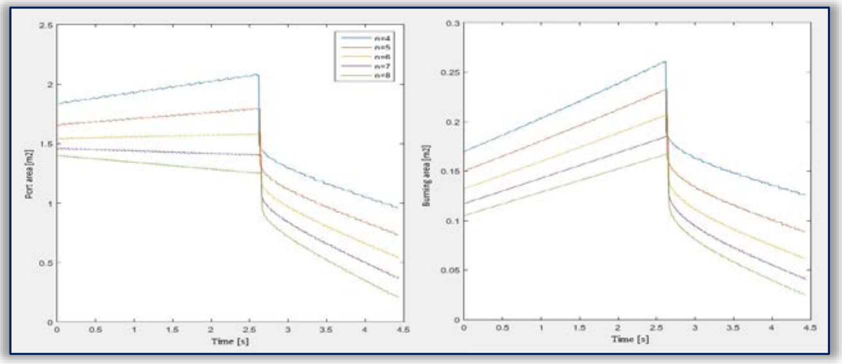

Figure 9. Port area variation with time for different star points number (left); burning surface variation with time for different star points number (right)

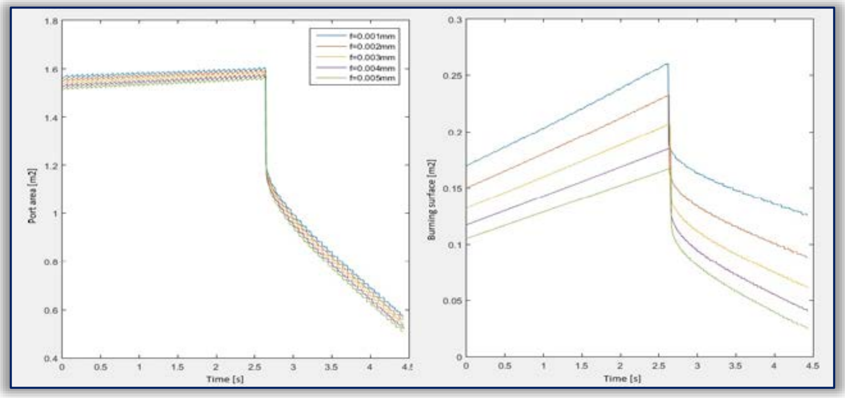

Figure 10. Port area variation with time for different grain section fillet radius values (left); burning surface variation with time for different grain section fillet radius values (right)

In Figure 10 – left, the port area variation with time is shown, for different grain section fillet values. As it can be seen, smaller fillet values lead to larger port areas. In Figure 10 – right, the burning surface variation with time is shown, for different grain section fillet values. As it can be seen, smaller fillet values lead to larger burning surface values.

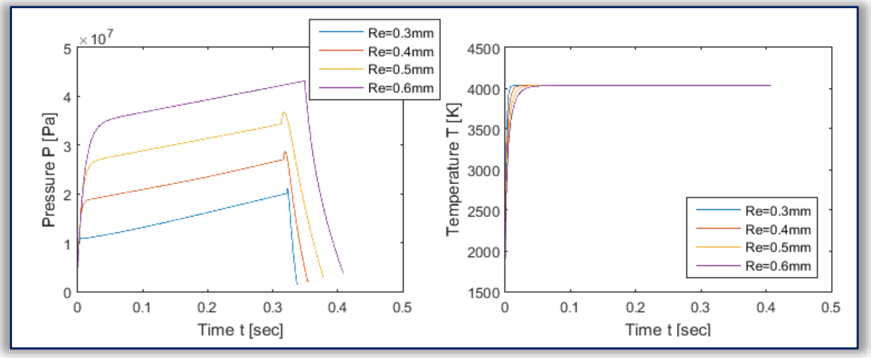

Figure 11. Pressure variation with time for different grain exterior radius values (left); temperature variation with time for different grain exterior radius values (right)

In Figure 11 – left, the chamber pressure variation with time is shown, for different grain exterior radius values. As it can be seen, larger grain exterior radius implies larger pressure values. In Figure 11 –right, the chamber pressure variation with time is shown, for different exterior radius values. As it can be seen, grain exterior radius has no influence on chamber pressure values.

In Figure 12 –left, the burn area variation with time is shown, for different grain exterior radius values. As it can be seen, larger exterior radius values imply larger burn areas and longer burn duration. In Figure 12 –right, the port area variation with time is shown, for different grain exterior radius values. As it can be seen, larger grain exterior radius values imply larger port areas.

In Figure 13 – left, the chamber volume variation with time is shown, for different grain exterior radius values. As it can be seen, larger exterior radius leads to larger chamber volume values. In Figure 13 – right, the grain burned thickness variation with time is shown, for different exterior radius values. As it can be seen, exterior radius values on grain burned thickness values.

In Figure 14 – left, the chamber pressure variation with time is shown, for different star points number. As it can be seen, star points number has no influence on chamber pressure, but leads to longer burn duration. In Figure 14 –right, the chamber pressure variation with time is shown, for different star points number. As it can be seen, star points number has no influence on chamber pressure values.

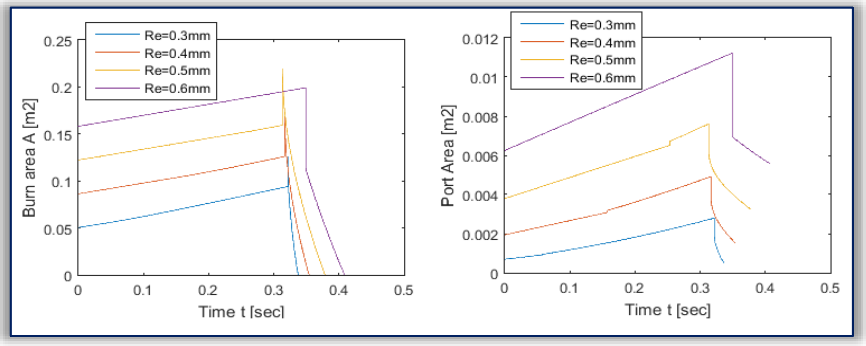

Figure 12. Burn area variation with time for different grain exterior radius values (left); port area variation with time for different grain exterior radius values (right)

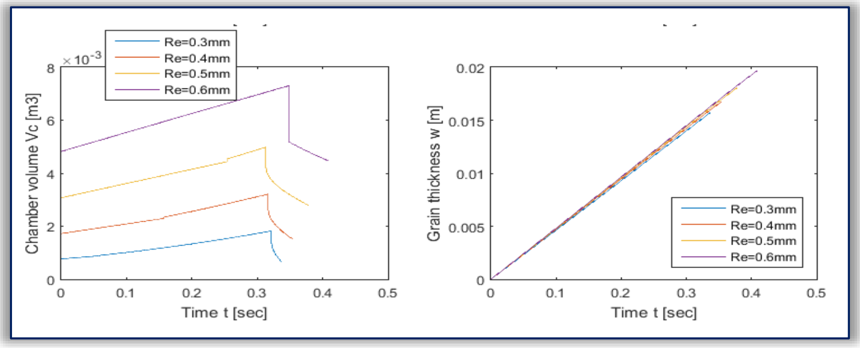

Figure 13. Chamber volume variation with time for different grain exterior radius values (left); grain burned thickness variation with time for different grain exterior radius values (right)

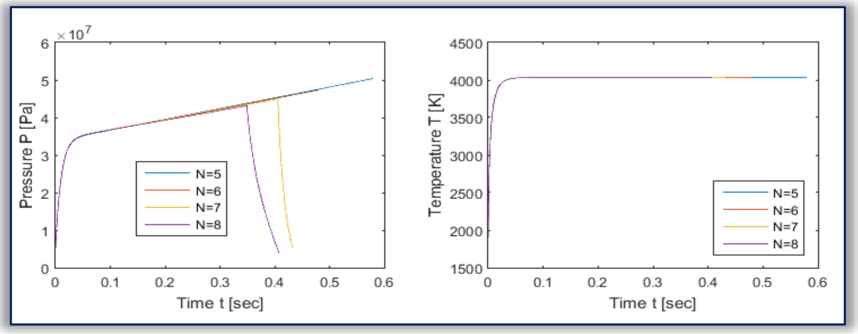

Figure 14. Pressure variation with time for different grain star points number (left); temperature variation with time for different grain star points number (right)

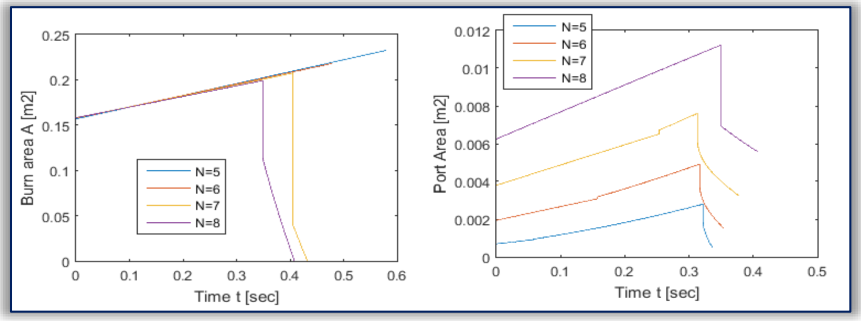

Figure 15. Burn area variation with time for different grain star points number (left); port area variation with time for different grain star points number (right)

In Figure 15 –left, the burn area variation with time is shown, for different number of star points. As it can be seen, more star points don't imply larger burn areas, but longer burn duration. In Figure 15 – right, the port area variation with time is shown, for different number of star points. As it can be seen, more star points imply larger port areas.

In Figure 16 – left, the chamber volume variation with time is shown, for different number of star points. As it can be seen, more star points lead to larger chamber volume values. In Figure 16 –right, the grain burned thickness variation with time is shown, for different number of star points. As it can be seen, number of star points has no influence on grain burned thickness values.

In Figure 17 – left, the chamber pressure variation with time is shown, for different grain lengths. As it can be seen, longer grains lead to larger chamber pressure values. In Figure 17 –right, the chamber temperature variation with time is shown, for different grain lengths. As it can be seen, grain length has no influence on chamber temperature values.

In Figure 18 –left, the burn area variation with time is shown, for different grain lengths. As it can be seen, longer grains imply larger burn areas. In Figure 18 – right, the port area variation with time is shown, for different grain lengths. As it can be seen, longer grains imply larger port areas.

In Figure 19 – left, the chamber volume variation with time is shown, for different SRM grain lengths. As it can be seen, for longer grain lengths, there are larger chamber volumes. In Figure 19 – right, the burned grain thickness variation with time is shown, for different grain lengths. As it can be seen, grain length has minimal influence on the thickness of burned grain.

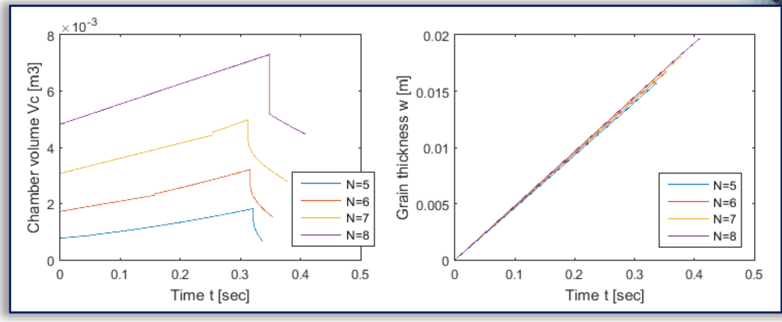

Figure 16. Chamber volume variation with time for different grain star points number (left); grain burned thickness variation with time for different grain star points number (right)

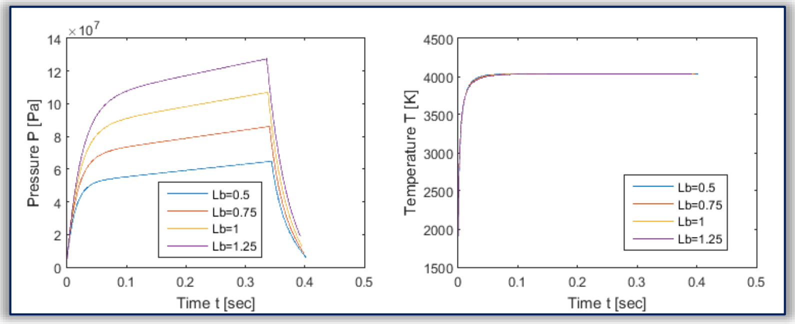

Figure 17. Pressure variation with time for different grain length values (left); temperature variation with time for different grain length values (right)

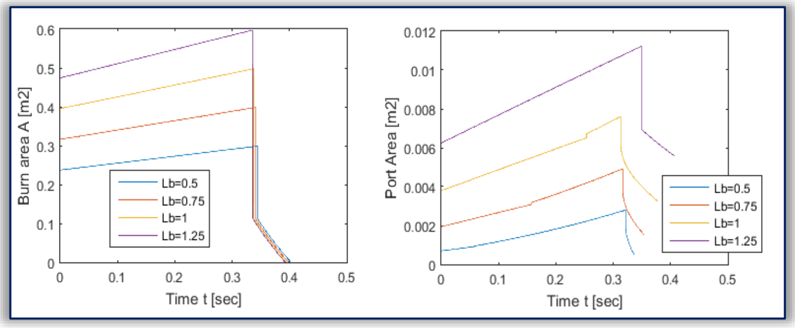

Figure 18. Burn area variation with time for different grain length values (left); port area variation with time for different grain length values (right)

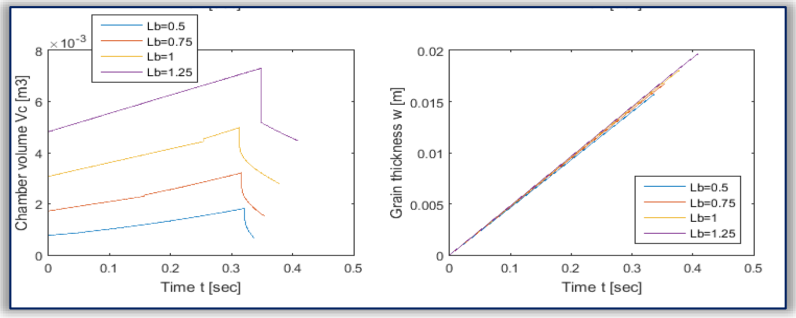

Figure 19. Chamber volume variation with time for different grain length values (left); grain burned thickness variation with time for different grain length values (right)

5. CONCLUSION

In this paper, a method of obtaining SRM star grain burning area and port area from a geometrical analysis was development. These areas were then used in the SRM internal ballistic model, and results were plotted for different star section geometrical parameters. Conclusions are set about the importance of each geometrical parameter in the performance of the SRM. Future work will include grain optimization for rocket mission constraints, and 1D SRM flow analysis.

REFERENCES

[1] H. Scheckar, Parametric Studies on Star Port Propellant Grain for Ballistic Evaluation, Defense Science Journal, Vol. 55, No. 4, October 2005, pp. 459-469, 2005, DESIDOC.
[2] M. F. Gomes, Internal Ballistics Simulation of a Solid Propellant Rocket Motor, UNIVERSIDADE DA BEIRA INTERIOR Engenharia, Covilha, Oct 2013.
[3] K O. Reddy, K M Pandey, Burnback Analysis of 3-D Star Grain Solid Propellant, International Journal of Advanced Trends in Computer Science and Engineering, Vol.2, No.1, Pages: 215-223 (2013) Special Issue of ICACSE 2013 - Held on 7-8 January, 2013 in Lords Institute of Engineering and Technology, Hyderabad, ISSN 2278-3091.
[4] R. C. HAINLINE, DESIGN OPTIMIZATION OF SOLID ROCKET MOTOR GRAINS FOR INTERNAL BALLISTIC PERFORMANCE, B.S. Southwest Missouri State University, 2006.
[5] A. P. Lorente, Study of Grain Burnback and Performance of Solid Rocket Motors, Escola Tehnica Superior d'Enginyeries Industrial i Aeronautica de Terassa, Universitat Politecnica de Catalunya, Jan. 2013.
[6] G. Puskulcu, Analysis of 3D Grain Burnback of Solid Propellant Rocket Motors and Verification with Rocket Motor Tests, The Graduate School of Natural and Applied Sciences of the Middle East Technical University, Aug. 2004.
[7] A. Lesage, Solid propellant grain geometry design, a model for the evolution of star shaped interfaces, Universiteit van Amsterdam, Faculteit der Exacte WetenSchappen, Aug. 9 2010.
[8] S.S. Dunn, D.E. Coats, 3-D Grain Design and Ballistic Analysis Using the SPP97 Code, Software and Engineering Associates, Inc. Carson City, NV, 1997.
[9] M. Johannsson, Optimization of Solid Rocket Grain Geometries, Deutsches Zentrum für Luft- und Raumfahrt e.V. Institut für Raumfahrtsysteme Systemanalyse Raumtransport (SART) 28359 Bremen, XR-EE-SPP 2012:002.
[10] P. Stalin, Y. N. V. S. Kumar, SK. Nazumuddin, Design and Geometrical Analysis of Propellant Grain Configurations of a Solid Rocket Motor, 2014 IJEDR | Volume 2, Issue 4 | ISSN: 2321-9939.

ANNALS of Faculty Engineering Hunedoara – International Journal of Engineering
ISSN 1584 - 2665 (printed version); ISSN 2601 - 2332 (online); ISSN-L 1584 - 2665